Applied Catalysis B: Environmental 320 (2023) 121938

Contents lists available at ScienceDirect

Applied Catalysis B: Environmental

journal homepage: www.elsevier.com/locate/apcatb

Pd/BEA hydrocarbon traps: Effect of hydrothermal aging on trapping properties and Pd speciation

Ryan P. Zelinsky [a], David P. Dean [b], Christian J. Breckner [b], Silvia Marino [a], Jeffrey T. Miller [b], William S. Epling [a,*]

[a] Department of Chemical Engineering, University of Virginia, Charlottesville, VA 22903, United States
[b] Davidson School of Chemical Engineering, Purdue University, West Lafayette, IN 47907, United States

ARTICLE INFO

Keywords:
Zeolites
Hydrocarbon trap
Hydrothermal aging
Emissions
Passive NO_x adsorption

ABSTRACT

Interest in Pd/zeolites as automobile exhaust catalysts has driven research focused on understanding the chemical environment of Pd active centers. Here, we studied the effects of hydrothermal deactivation on a Pd/BEA hydrocarbon trap. Hydrothermal aging (HTA) led to decreased ethylene storage capacity and oxidation activity. Characterization by x-ray absorption spectroscopy (XAS) and NO_x adsorption indicated that for lower Si/Al ratio samples, the amount of ion exchanged Pd increased after HTA. Temperature programmed desorption of NO_x after NO exposure revealed two desorption peaks, with a high temperature peak that increased in area with increased aging temperature. Based on infrared spectroscopy, XAS and reactor results, the high temperature desorption peak is consistent with NO stored on Pd^{+}. The Pd^{+} formed during NO adsorption, existing originally as $[Pd(OH)]^{+}$. This species was less active in ethylene storage and oxidation than the original Pd^{2+} species. $[Pd(OH)]^{+}$ stored NO_x to a higher temperature than Pd^{2+}.

1. Introduction

As advances are made in diesel engine design and control, exhaust aftertreatment technologies must continue to meet the environmental regulatory requirements. More efficient compression ignition technologies, such as Low Temperature Combustion (LTC), offer higher fuel efficiency but suffer from markedly higher CO and hydrocarbon emissions [1–3]. In addition, the exhaust gases are at lower temperatures, which will put more stress on a conventional diesel oxidation catalyst (DOC) to reduce these emissions to an acceptable level.

Another source of unburned hydrocarbon emissions is the cold-start phase of vehicle operation, which can contribute up to 60–80% of the total hydrocarbon emissions for current combustion technologies [4–6]. Currently, there is ongoing research in improving the low temperature activity of DOCs [7]; however, alternative technologies are also being developed to address these low exhaust temperature hydrocarbon emissions. Of these, the hydrocarbon trap is of particular interest. An effective hydrocarbon trap must adsorb hydrocarbons at low temperatures (ambient to 200 °C) and oxidize them or release them to be oxidized downstream at temperatures above the working temperature of the DOC. That working temperature varies with the target hydrocarbon. For example, for short chain alkanes, the needed temperature for the onset of oxidation over a Pt-based catalyst decreases with increasing chain length, and alkenes are typically easier to oxidize than alkanes [8,9].

Zeolites are typically chosen as the support material for hydrocarbon traps due to their pore size range and properties as solid acids [10–13]. Zeolites in the proton form suffer due to competitive adsorption by water inhibiting uptake of small chain unsaturated hydrocarbons such as ethylene or propylene [13–15]. To solve this, the zeolites can support/exchange metal active sites which adsorb hydrocarbons in the presence of water [16–19]. Recent studies have highlighted zeolites exchanged with metals including Ag [20–22], Pd [23–30], and Cu [31,32] as potential candidates for low temperature hydrocarbon traps. Of these, zeolites with ion exchanged Pd are of special interest as they are currently the subject of study for many applications in addition to hydrocarbon trapping including methane oxidation [33,34], Wacker oxidation [35,36], and as passive NO_x absorbers (PNA) [37–45]. The hydrocarbon oxidation activity of Pd, as well as its ability to adsorb unsaturated hydrocarbons under vehicle exhaust conditions, makes it an attractive active metal for hydrocarbon traps [26–28].

For this application, the impact of CO and H_2O exposure is of

* Corresponding author.
E-mail address: wse2t@virginia.edu (W.S. Epling).

https://doi.org/10.1016/j.apcatb.2022.121938
Received 26 June 2022; Received in revised form 30 August 2022; Accepted 1 September 2022
Available online 6 September 2022

particular interest as these are combustion products which are always present in diesel exhaust. Vu et al. studied the effect of CO on a Pd/BEA PNA. They highlighted an increase in NO adsorption capacity and an increase in desorption temperature with increased CO feed concentration [46]. It was further clarified by Zheng et al. that the presence of CO may not increase the total NO adsorption capacity, but rather increase the adsorption rate which in turn reduces the competitive adsorption effects of H_2O [41]. Previously, we showed that although dodecane uptake was not influenced, ethylene uptake was reduced by 90 % over Pd/BEA when comparing uptake under dry, CO-free conditions to conditions containing CO and H_2O [24]. These reports suggest that CO can have a positive effect on PNA performance but a detrimental effect on hydrocarbon trap performance.

Other findings have focused on Pd speciation and how exposure to CO may affect that speciation and distribution of Pd site types. For example, high temperature CO exposure was reported to induce reduction of Pd^{2+} active sites and agglomeration of Pd^0 particles in various Pd/zeolites, resulting in a decrease in PNA performance [47,48]. Some Pd/zeolite PNA studies noted that including CO during the cycling between low temperature NO adsorption followed by exposure to high temperatures to desorb the NO can lead to a loss of ion-exchanged Pd [39,49]. Recently, low temperature reduction of ionic Pd^{2+} by CO was observed by IR spectroscopy over Pd/BEA [24] and Pd/SSZ-13 [50]. The reduction occurs at lower temperatures in the presence of H_2O, suggesting that hydration of Pd ions is an important step in their reduction at low temperature [50].

Another method of deactivation is by hydrothermal aging (HTA), which is meant to simulate time-on-stream degradation of an aftertreatment catalyst. Ryou et al. found that HTA at 750 °C for 25 h led to an increase in PNA performance due to redistribution of PdO into highly dispersed and NO adsorption active Pd^{2+} [51]. Lee et al. reported that the change in Pd speciation during HTA at 750 °C for 25 h depended on the zeolite framework, with Pd ions more mobile in the larger pore ZSM-5 versus SSZ-13. In their case, with an initially high dispersion of ion-exchanged Pd, HTA led to more significant deactivation for the larger pore Pd/zeolites [52]. Indeed, the zeolite framework, the Si/Al ratio, the Pd loading, and many other conditions may affect Pd speciation and catalyst deactivation after HTA.

Herein, we investigate changes in Pd speciation over Pd/BEA of three different Si/Al ratios after HTA at 550, 600, and 650 °C. This effort combines ethylene and NO_x trapping flow reactor experiments with diffuse reflectance Fourier transform infrared spectroscopy (DRIFTS) and X-ray adsorption spectroscopy (XAS) to characterize the Pd speciation before and after the HTA treatments. Ethylene and NO_x trapping experiments revealed changes in the storage capacity and oxidation activity of Pd/BEA, while DRIFTS and XAS studies aided in identifying changes in Pd speciation during CO/NO exposure in H_2O-containing atmospheres.

2. Experimental methods

2.1. Synthesis and aging

Zeolite beta powder was purchased from Zeolyst (SiAl = 12.5 and 19) and ACS Material (SiAl = 75). The catalysts with SiAl = 12.5 and 19 were acquired in the NH_4^+ cation form, while the SiAl = 75 catalyst was in the H^+ cation form. All three powders were calcined at 500 °C for 4 h in air to obtain the common H^+ form. Pd was added to the catalyst to attain a 0.5 wt% loading by a modified ion-exchange method, adapted from the method described by Khivantsev et al. [53]. A nominal amount of $Pd(NO_3)_2$ (Sigma Aldrich) as a precursor was dissolved in 28% aqueous ammonia (Sigma Aldrich) and then mixed with the zeolite powder. The slurry was stirred vigorously for 10 min with a glass stirring rod and then placed in a furnace to dry in air at 120 °C for 2 h. The Pd/BEA was then calcined at 600 °C for 4 h in air. Aged catalysts were prepared from the fresh catalysts by high temperature exposure to a gas mixture containing 1000 ppm CO, 5% H_2O, 10% O_2 and balance N_2 at 550, 600, and 650 °C for 24 h. In this manuscript, the catalysts will be referred for example as PdBEAXY where the XY corresponds to the Si/Al ratio.

2.2. Catalyst evaluation

Low temperature ethylene and NO_x trapping experiments were conducted on a benchtop reactor system. Ethylene was used as the probe molecule in this study, as it is a representative small chain alkene, representative long chain alkanes do not show interesting behavior dependent on the ion-exchanged metal, and there seems to be interesting ethylene uptake and oxidation behavior dependent on the ion-exchange properties [21]. The Pd/BEA samples were sieved to obtain particles between 40 and 60 mesh (250–400 μm). Then, 40 mg of sieved catalyst powder was placed into 0.25-inch ID quartz tubes (Quartz Scientific) between two sections of quartz wool. The tubes were then placed into a Thermo Fisher Scientific Lindberg Blue M tube furnace with K-type thermocouples placed in the upstream and downstream ends of the catalyst bed. To produce the gas mixture, gas cylinders were purchased from Praxair and the flow rates of all except steam and its N_2 carrier were controlled using MKS Instruments mass flow controllers. Water was supplied to the gas phase using a Bronkhorst controlled evaporator mixer. The flow rate for all experiments and aging treatments was 550 sccm. This corresponds to a space velocity of 50,000 hr^{-1}, calculated based on the flow conditions of a monolith. Specifically, the catalyst mass (40 mg) was calculated by dividing the total flow rate (550 sccm) by the desired space velocity (50,000 hr^{-1}) and then multiplying the resulting volume by a nominal monolith catalyst loading of 1 g/in^3. Reported reactor outlet gas phase concentrations were measured using an MKS MG2030 IR analyzer. Table 1 shows the concentrations of gases in the reactant mixture used in each experiment. Gas concentrations were verified through a bypass line before being introduced to the catalyst.

Each hydrocarbon and NO_x trapping experiment began with a pretreatment in 10 % O_2/N_2 at 600 °C for 1 h to oxidize any residual carbon and establish a normalized starting point for each experiment. Next, the catalyst was cooled to 80 °C in 10 % O_2/N_2 while the reactant gas mixture was established in the bypass. Once 80 °C was reached and unchanging, the reactant gas mixture was switched to the reactor and the catalyst was exposed to it for 30 min. Then, during the subsequent temperature programmed desorption (TPD) or oxidation (TPO), the temperature was ramped from 80° to 600 °C at a rate of 20 °C/min. Ethylene uptake was calculated with data from the adsorption phase because during TPO most of the ethylene was oxidized to CO and CO_2. NO_x uptake, however, was calculated from the desorption phase as all NO_x desorbed as NO or NO_2.

2.3. Catalyst characterization

2.3.1. XRD

X-ray diffraction (XRD) was used to determine the crystallinity of the fresh catalyst and confirm a retained zeolite beta structure. XRD

Table 1
Experimental gas phase concentrations.

	Gas concentration					
Experiment	CO	NO	C_2H_4	H_2O	O_2	N_2
Ethylene Adsorption	0	0	200 ppm	5 %	10 %	balance
NO Adsorption	0	200 ppm	0	5 %	10 %	balance
CO/H_2O Pretreatment	500 ppm	0	0	5 %	10 %	balance
HTA w/ CO	1000 ppm	0	0	5 %	10 %	balance

experiments were conducted using an Empyrean multipurpose X-ray diffractometer equipped with a line-focus Cu anode X-ray source and a GaliPIX3D detector. XRD patterns are shown in the supplementary information in Fig. S1.

2.3.2. XAS

Pd K-edge (23,450 eV) X-ray adsorption spectra were collected over fresh and aged Pd/BEA samples at the 10-BM-B beamline at the Advanced Photon Source at Argonne National Laboratory. The catalyst powder was ground and sieved to particle sizes less than 250 μm and packed into one of six wells in a stainless-steel sample holder. The sample holder was placed into a 1-inch ID tube and sealed within an air-tight cell with valves allowing for gas flow [54]. The samples were pretreated at 600 °C in 10% O_2/He for 1 h, then cooled to 80 °C. The tube was transferred to the beamline and exposed to reaction conditions, where in-situ XAS measurements were taken. The data were normalized and the edge energy was calibrated using the Athena software from the Demeter XAS analysis package. EXAFS spectra were fit, and parameters calculated, in the Artemis program of the same software package.

2.3.3. DRIFTS

Catalysts were also characterized using diffuse reflectance infrared Fourier transform spectroscopy (DRIFTS) during CO and NO exposure to investigate Pd speciation. The samples were placed in a Harrick Scientific Praying Mantis reaction chamber equipped with ZnSe windows. The cell was then loaded into a Nicolet iS50 FT-IR spectrometer. A 500 °C pretreatment in 10% O_2/He preceded each experiment. Next, the catalyst was cooled to 80 °C in 10% O_2/He. Then, a background spectrum was taken in pure He, or in the case of a water-containing experiment, 1.6% H_2O/He. Finally, the catalysts were exposed to 1000 ppm CO or 700 ppm NO and spectra were collected, with 32 spectra averaged for each reported spectrum at a resolution of 4 cm^{-1}.

3. Results and discussion

3.1. Ethylene trapping and TPO

Ethylene adsorption experiments were performed to evaluate the hydrocarbon trapping efficacy of the fresh and aged catalysts. The results for PdBEA19 are shown in Fig. 1. These data show a decline in ethylene adsorption capacity with increasing aging temperature. This trend held for Pd/BEA catalysts of each Si/Al ratio, as summarized in Table 2. In the presence of water, ethylene uptake will occur mainly on Pd sites, as water will competitively adsorb to the zeolite's Brønsted acid sites [13–15]. For each sample, the total amount of stored ethylene was up to four times the amount of Pd in the catalyst. This indicates that ethylene is not stored as isolated molecules, but rather is activated by Pd and oligomerizes into higher molecular weight deposits, as has been shown to occur over Pd-containing zeolites as well as other metal exchanged zeolites at similar temperatures as those used here [27,55]. As seen in Fig. 1, the outlet ethylene concentration did not return to the inlet value over the course of the adsorption phase. This is because a small amount of ethylene is continually reacting at oligomerization sites, allowing additional ethylene uptake.

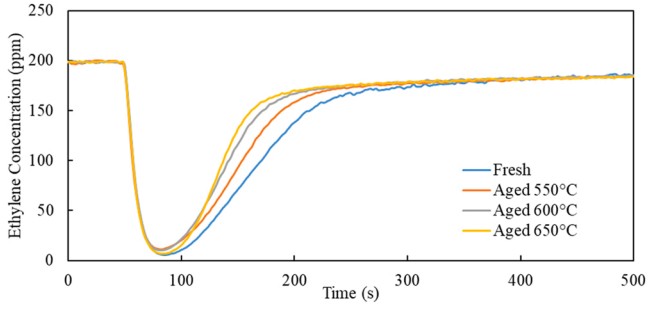

Fig. 1. Ethylene adsorption over PdBEA19 before and after HTA for 24 h in 1000 ppm CO, 10 % O_2, 5 % H_2O and balance N_2. The reactant mixture during adsorption contained 200 ppm C_2H_4, 10 % O_2, 5% H_2O and balance N_2. The ethylene-containing gas mixture was switched to the reactor from the bypass at t = 50 s and the sample was exposed to this mixture at 80 °C for 30 min.

Ethylene oxidation conversion as a function of temperature, Fig. 2, was also impacted by the aging treatments, with increasing temperatures needed to achieve the same conversions as aging temperature increased. Additionally, at low conversion, acetaldehyde was formed over both the fresh and aged samples, with the data obtained from the fresh sample shown in Fig. 2 and from both the fresh and aged at 650 °C samples shown in Fig. S2. This can be explained by the presence of ongoing Wacker-type chemistry. In Wacker oxidation, ethylene is converted to acetaldehyde through a catalytic redox cycle. Heterogenous Pd-containing Wacker catalysts have been demonstrated in recent work, where zeolite-supported Pd active sites cycle between Pd^0 and Pd^{2+}, aided by Cu^{2+} ions [35,36]. The presence of Wacker oxidation suggests the existence of Pd^{2+} ions in both the fresh and aged samples. The formation of these byproducts might also explain the inflection in the conversion as a function of temperature plot, via inhibition by CO and acetaldehyde.

3.2. NO_x Adsorption

Degradation in both ethylene uptake capacity and ethylene oxidation activity points towards deactivation induced by HTA. One deactivation mode is a loss in Pd active sites via agglomeration or migration out of the zeolite pores during aging. The presence of Wacker chemistry implies the existence of some Pd^{2+} in each sample, but does not quantify the amount. So, to investigate loss of Pd dispersion as a possible cause of deactivation, the amount of ionic Pd was quantified before and after aging.

The presence of dispersed ionic Pd can be tested and quantified by the amount of NO that adsorbs during a NO_x adsorption experiment, as atomically dispersed Pd^{n+} (n = 1,2) is widely regarded as the active adsorption site in Pd/zeolite PNAs [37–40,53,56–59]. With this in mind, we exposed each catalyst to 200 ppm NO, 5 % H_2O, 10 % O_2, and balance N_2 at 80 °C for 30 min, then performed a TPD in the presence of the same gas mixture while measuring the outlet NO_x concentration. Table 3 shows the NO_x-to-Pd ratio, with NO_x storage measured by the amount of NO_x that desorbed during the TPD phase, for each catalyst. The NO_x storage capacity increased with increasing aging severity for PdBEA12.5 and PdBEA19, and remained the same after aging for PdBEA75. This shows that after the initial synthesis, not all Pd was available to adsorb NO, but with aging the amount available increased.

The increase in NO_x storage capacity rules out a loss in ionic Pd, but rather points to an increase in exchanged Pd after aging. The redistribution of bulk PdO into highly dispersed Pd^{2+} after HTA has been previously reported for both Pd/SSZ-13 [51] and Pd/ZSM-5 [52]. The relative lower concentration of zeolite Al^- sites likely explains why the highest Si/Al ratio zeolite did not see improvement in Pd dispersion after HTA, unlike the lower Si/Al ratio zeolites.

3.3. Characterization by XAS

To further characterize the chemical environment of the Pd before and after aging, XAS measurements at the Pd K-edge were carried out on the fresh catalysts of all three Si/Al ratios, and on the aged samples with SiAl = 19. Prior to measurement, each sample was oxidized in 10% O_2/He for 1 h at 600 °C. Fig. 3 shows the magnitude of the Fourier-transformed EXAFS spectra, taken in He at 80 °C, for the fresh and aged catalysts. In each sample, we observe a feature at R = 2.4 Å. This is due to second shell Pd-O-Si(Al) scattering associated with the zeolite framework, and its presence implies that some of the Pd is tightly associated with the framework ion-exchange sites [37].

Table 2
Ethylene adsorbed during a 30 min ethylene exposure and the temperature at which 50% conversion is achieved, T_{50}, during the subsequent temperature programmed oxidation.

	Ethylene:Pd Ratio (total uptakes listed also)			Oxidation T_{50} (°C)		
	PdBEA12.5	PdBEA19	PdBEA75	PdBEA12.5	PdBEA19	PdBEA75
Fresh	3.9 (7.9)	4 (8.0)	3.4 (6.7)	305	301	326
550 °C	4.1 (8.0)	3.9 (7.5)	–	372	347	–
600 °C	3.9 (7.5)	3.5 (6.8)	–	387	361	–
650 °C	3.7 (7.3)	3.3 (6.6)	2 (3.8)	397	382	381

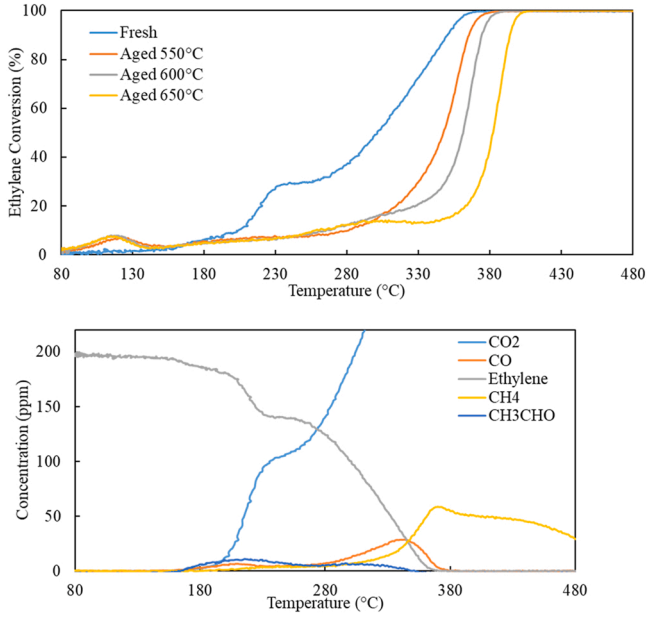

Fig. 2. Top panel: Ethylene conversion over PdBEA19 before and after HTA for 24 h in 1000 ppm CO, 10 % O_2, 5 % H_2O and balance N_2. Bottom panel: Outlet gas phase concentration traces for several gas phase species in the effluent during ethylene TPO over the fresh PdBEA19 sample. The reactant mixture during the temperature ramp contained 200 ppm C_2H_4, 10 % O_2, 5 % H_2O and balance N_2. The ramp rate was 20 °C/min.

Table 3
NO_x:Pd ratio and amount of NO_2 observed during the NO exposure at 80 °C.

	NO_x:Pd (Desorption)	NO_2 Formed (μmol)[a]
Fresh PdBEA12.5	0.42	0.12
Aged 550 °C	0.52	0.33
Aged 600 °C	0.58	0.43
Aged 650 °C	0.60	0.57
Fresh PdBEA19	0.19	0.01
Aged 550 °C	0.52	0.23
Aged 600 °C	0.53	0.27
Aged 650 °C	0.58	0.42
Fresh PdBEA75	0.23	0.04
Aged 650 °C	0.23	0.06

[a] Calculated during the adsorption of NO at 80 °C.

In the fresh catalysts, a coordination number (CN) of 3.8–3.9 for Pd-O scattering was calculated for all three samples, suggesting that the samples were fully oxidized to Pd^{2+} by the oxygen pretreatment. The samples also displayed second shell Pd-O-Pd scattering around R = 3 Å, which is characteristic of bulk PdO_x [60]. The PdBEA75 sample displayed the highest intensity of second shell scattering, indicating that a more significant fraction of the Pd in this sample existed as PdO particles. During synthesis, the amount of exchanged Pd did not exceed the maximum theoretical limit for ion exchange for these catalysts, as shown by the calculation in the SI, Table S1, but the relative lower concentration of Al^- sites in the SiAl = 75 catalyst may have played a role in its reduced Pd dispersion. The SiAl = 12.5 and 19 catalysts displayed a lower intensity of second shell Pd-O-Pd scattering, implying that for these samples a smaller fraction of Pd exists as bulk PdO_x. EXAFS spectra for Pd/SiO_2 and $Pd(OAc)_2$ are provided in Fig. S3 as standards for bulk PdO and isolated Pd^{2+}, respectively.

For all three of the aged PdBEA19 samples, the Pd-O scattering path CN was calculated to be between 4.0 and 4.1. Additionally, over all three samples no second shell Pd-O-Pd scattering was observed. This indicates that HTA under these conditions did not promote the formation of bulk PdO_x, and rather, aging may have increased Pd dispersion as suggested above by the NO_x storage results. From this, we infer that the Pd exists mainly as ion-exchanged Pd in the aged samples, and that any bulk PdO_x exists as a minor phase outside the detection limits of XAS. The EXAFS fittings for fresh and aged catalysts are reported in Table S2.

3.4. NO_x TPD

Although ionic Pd was not lost after the aging treatments, the behavior of both ethylene storage and NO_x storage did change, with a decrease in the former and an increase in the latter. This shows that the Pd remains in an ionic state, but HTA conditions promote the formation of additional ionic Pd species that are preferable for NO_x storage and less active in ethylene oligomerization and oxidation. NO_x TPD can be used to track changes in Pd speciation, as different Pd storage sites can desorb NO_x at different temperatures depending on the strength of the bonds formed.

The NO_x TPD results, Fig. 4, show trends in NO_x desorption behavior with aging that vary with Si/Al ratio. The fresh PdBEA12.5 sample displays a NO_x desorption peak centered at ~135 °C, while the aged samples contain both the peak at 135 °C and an additional desorption feature with a peak in amount released at 230 °C, which grows with increased aging temperature. The PdBEA19 catalyst displayed a similar behavior, with the peak at 230 °C growing with increased aging temperature. In the highest Si/Al ratio, PdBEA75, only the peak at 135 °C exists in both the fresh and aged catalysts. The increase in NO_x release at 230 °C on the aged catalysts of low Si/Al suggests that HTA promotes the formation of a Pd species which stores NO_x to higher temperatures.

3.5. Identification of Pd active sites

To aid in identifying the potential NO_x storage site, we first discuss how Pd is ion-exchanged into the zeolite. During a high temperature oxidative treatment, it has been proposed that PdO monomers interact with Brønsted acid sites to form ion-exchanged Pd^{2+} in a process called "protonolysis" as described by Adelman and Sachtler [61].

$$PdO + 2\ H^+Z^- \rightarrow Z^-Pd^{2+}Z^- + H_2O \quad (1)$$

Mei et al. [40] noted that the PdO monomer may also interact with a single Brønsted acid proton to form $Z^-[Pd(OH)]^+$.

$$PdO + H^+Z^- \rightarrow Z^-[Pd(OH)]^+ \quad (2)$$

IR spectroscopic studies using CO as the probe molecule provide further evidence that multiple ionic Pd^{n+} sites exist in Pd/BEA [41,47,

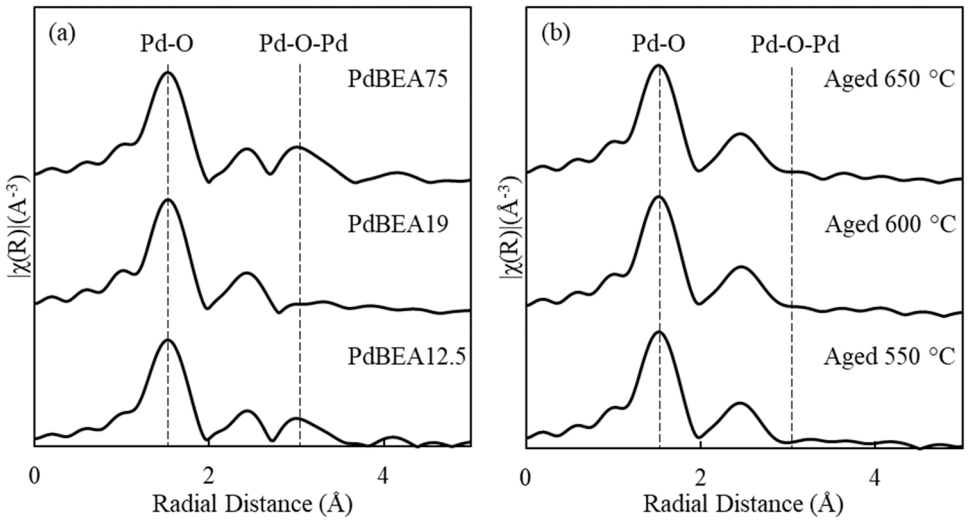

Fig. 3. Magnitude of the Fourier transformed EXAFS spectra recorded over PdBEA during exposure to He at 80 °C after pretreatment in 10 % O_2 at 600 °C. (a) Fresh PdBEA of three Si/Al ratios. (b) Aged PdBEA19 at the three aging temperatures.

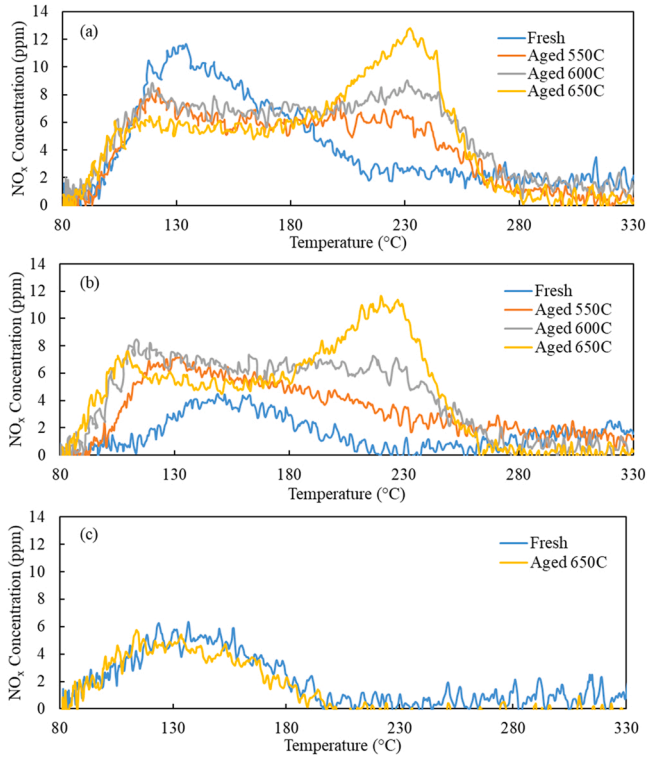

Fig. 4. NO_x TPD over (a) PdBEA12.5, (b) PdBEA19, and (c) PdBEA75 before and after HTA for 24 h in 1000 ppm CO, 10% O_2, 5% H_2O and balance N_2. The reactant mixture during temperature ramp contained 200 ppm NO, 10% O_2, 5% H_2O and balance N_2. The ramp rate was 20 °C/min.

62]. Due to the formation of NO_2 during the initial adsorption of NO, many authors have suggested a mechanism wherein Pd^{2+}, in the form of $[Pd(OH)]^+$, is reduced to Pd^+ by NO, as described by reaction (3) [40,41,53,56,58,63,64].

$$2Z^-[Pd(OH)]^+ + NO \rightarrow 2Z^-Pd^+ + NO_2 + H_2O \quad (3)$$

This pathway requires two $Z^-[Pd(OH)]^+$ sites in proximity because of the two electron requirement to oxidize NO to NO_2 [41]. The stoichiometry of this pathway also yields a theoretical NO_2 released:NO stored ratio of 0.5, assuming all Pd sites are in the form of $Z^-[Pd(OH)]^+$, and NO storage occurs via reaction (4).

$$Z^-Pd^+ + NO \rightarrow Z^-Pd^+(NO) \quad (4)$$

And overall:

$$2Z^-[Pd(OH)]^+ + 3NO \rightarrow 2Z^-Pd^+(NO) + NO_2 + H_2O \quad (5)$$

In this work, we observed the formation of NO_2 during the adsorption phase of the NO_x trapping experiments, Fig. S4. Note, N_2O was not observed in any experiment. The amount of NO_2 formed during adsorption increased with increasing aging temperature, Table 3. Due to the low adsorption temperatures involved, 80 °C, and the transient nature of the NO_2 signal, catalytic NO oxidation to NO_2 is unlikely. Thus, we propose that this NO_2 formation occurs via stoichiometric reduction of $[Pd(OH)]^+$ as outlined in Eq. (3), and based on this reaction, NO_2 formation might be a selective measure of $[Pd(OH)]^+$.

Analysis of the NO_2 released during adsorption versus NO stored for all samples, Fig. 5, shows that aging increases the ratio of NO_2 formed to NO stored (shortened to NO_2:NO from here on), and this value approaches the theoretical limit of 0.5, set by the stoichiometry of Eq. (5).

As detailed in reaction (5) above, the theoretical NO_2:NO of 0.5 implies that all Pd which is active in NO_x storage is in the form of $Z^-[Pd(OH)]^+$. Due to the trends we observe in this ratio, and the coinciding increase in the relative area of the high temperature NO_x desorption peak with increased aging temperature, we assign this NO desorbing at

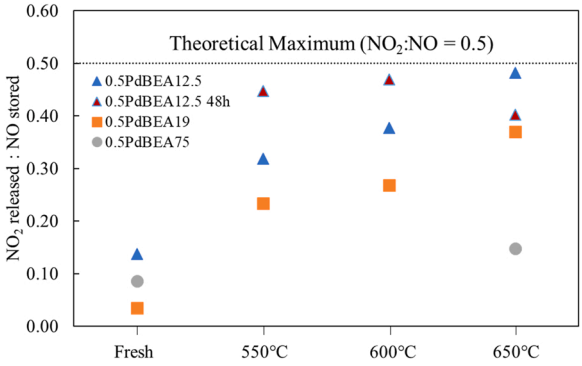

Fig. 5. NO_2 released:NO stored for each catalyst. NO_2 released measured during adsorption of NO at 80 °C. NO stored measured as NO_x desorbed during TPD. Feed: 200 ppm NO, 10% O_2, 5% H_2O, balance N_2. Ramp rate = 20 °C/min.

higher temperature to NO that was stored on Z^-Pd^+. With this assignment, it follows that HTA promotes the formation of $Z^-[Pd(OH)]^+$. The formation of this species during HTA may be from bulk PdO_x, as suggested by the above characterization, or by transformation of $Z^-Pd^{2+}Z^-$, or a combination of both. We note that the ratio did not reach the theoretical value of 0.5, which would be the case if all the Pd that stored NO was in the $[Pd(OH)]^+$ form, indicating that there are other Pd species available to adsorb NO.

To further verify this assertion, extended aging (48 h) was conducted on the PdBEA12.5 catalyst. NO_x storage experiments yielded NO_2:NO ratios closer to 0.5 for 550 and 600 °C aging for 48 h, shown in Fig. 5 (values shown in Table S3). Aging at 650 °C for 48 h decreased this ratio slightly, but this may be due to dealumination from extended exposure to hydrothermal conditions [65]. Dealumination would reduce the total amount of Al^- sites in the zeolite, and thus remove potential nearby Pd sites which enable the redox chemistry to occur.

The Si/Al ratio of the zeolite also had an effect on the Pd speciation changes during aging. The PdBEA12.5 catalyst most closely approached the theoretical NO_2:NO ratio, while the highest Si/Al ratio catalyst, PdBEA75, which did not display a NO_x desorption peak at 230 °C, displayed the lowest NO_2:NO ratio after aging at 650 °C. This difference is due to the relative concentration of nearby Al^- sites. As stated above, the chemistry requires two $Z^-[Pd(OH)]^+$ sites to be reduced by one NO molecule, resulting in the formation of one NO_2 molecule. If there are fewer total Al^- substitutions, as in the case of the highest Si/Al catalyst, then the amount of nearby Al^- sites will also be lower, limiting the this chemistry. The inability to form reducible pairs of $Z^-[Pd(OH)]^+$ may also explain why only the PdBEA75 catalyst did not improve in NO_x storage capacity after HTA.

3.6. Effect of CO and H_2O pretreatment on NO_x TPD

With the assignment of the high temperature NO desorption peak to NO stored on Z^-Pd^+, we turn attention to the identity of the low temperature NO_x desorption peak, which exists in both the fresh and aged samples. Since $[Pd(OH)]^+$ is a reducible species, the non-reducible NO_x storage sites can be isolated by a reductive pretreatment. Note, we have run similar experiments to those described below, but with H_2 instead of CO. The addition of H_2 led to no change relative to the experiment in its absence.

In a previous study, we reported that a reduced Pd phase on Pd/BEA appears in CO DRIFTS when CO and H_2O are both present in the reactant gas at 80 °C. This does not occur with just CO in the absence of H_2O [24]. This was further clarified by Song et al. [50] to be the reduction of ionic Pd^{n+} via CO aided by H_2O solvation. Taking advantage of this phenomenon, we subjected the PdBEA12.5 (aged at 650 °C) sample to a CO + H_2O pretreatment at 80 °C for 1 h. This serves to eliminate the reducible $[Pd(OH)]^+$ species and leave behind only $Z^-Pd^{2+}Z^-$ ions, which are not reducible by CO under these conditions [41,50]. After the CO + H_2O pretreatment, the standard NO_x adsorption followed by TPD experiment was performed. Table 4 shows the amount of NO_x stored and NO_2 formed during adsorption for this experiment and the control without a CO + H_2O pretreatment. Here we observe a fourfold loss in NO_2 formation, demonstrating that CO had reduced most of the $[Pd(OH)]^+$ during the pretreatment.

Fig. 6 shows the TPD results for NO adsorption with and without the CO + H_2O pretreatment. The NO_x TPD on the sample exposed to the CO + H_2O pretreatment (black) contains only one desorption feature,

Table 4
NO_x Storage and NO_2 formation over PdBEA12.5 Aged 650 ° with and without a CO + H_2O pretreatment.

PdBEA12.5 Aged 650 °C	NO_x:Pd	NO_2 Formation (μmol)	Ratio of NO_2:NO
No CO Pretreatment	0.60	0.57	0.48
Wet CO Pretreatment	0.44	0.13	0.15

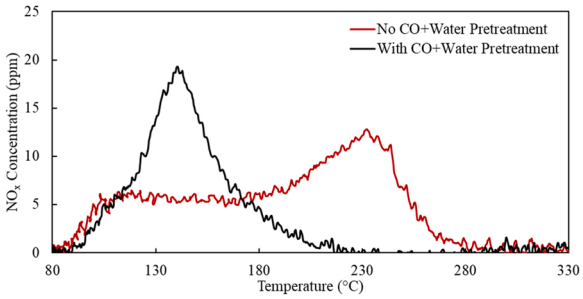

Fig. 6. NO_x TPD over PdBEA12.5 after the 650 °C exposure containing 1000 ppm CO, 10% O_2, 5% H_2O and balance N_2. The black line indicates the NO_x TPD after an 80 °C exposure to 500 ppm CO, 5% H_2O, 10% O_2 and balance N_2. The reactant mixture during temperature ramp contained 200 ppm NO, 10% O_2, 5% H_2O and balance N_2. The ramp rate was 20 °C/min.

centered around ~135 °C. The loss of the desorption peak centered at 230 °C is attributed to the reduction of $[Pd(OH)]^+$ to Pd^0 during the CO + H_2O pretreatment. Since the first desorption peak centered around ~135 °C was not lost under these conditions, it is likely associated with NO_x stored on $Z^-Pd^{2+}Z^-$. The fact that the peak grows after CO + H_2O exposure, however, indicates that either more Pd^{2+} was formed potentially due to reoxidation of Pd^0 by O_2 between CO and NO exposures, or that an additional species which adsorbs NO has formed.

3.7. CO DRIFTS

To further clarify the state of the Pd after the CO + H_2O pretreatment, and help explain the results shown in Fig. 6, two experiments were conducted using DRIFTS. In the first, Fig. 7a, PdBEA12.5 was exposed to 1000 ppm CO in He at 80 °C. In the second, Fig. 7b, the catalyst was exposed to 1000 ppm CO and 1.6% H_2O in He at 80 °C.

We observe in Fig. 7 several peaks corresponding to CO bound to Pd^{n+}. In spectrum (a), the peaks at 2214 and 2194 cm^{-1} are assigned to CO bound to super electrophilic Pd^{2+}, as reported by Khivantsev et al. [66]. These species, along with those associated with peaks at 2180 and 2171 cm^{-1} are absent in spectrum (b), and are thus unstable in the presence of CO and H_2O. The peak at 2180 cm^{-1} has been previously assigned to CO-$[Pd(OH)]^+$ by Zheng et al. [41]. The peak at 2171 cm^{-1} was also removed upon CO + H_2O adsorption, but may be assigned to CO adsorbed onto Brønsted acid sites and not related to Pd [67]. A peak

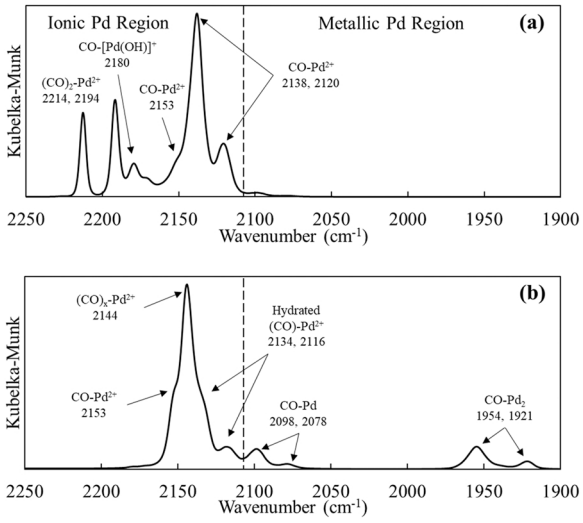

Fig. 7. CO DRIFTS spectra collected over PdBEA12.5 after 30 min exposure at 80 °C to 1000 ppm CO in (a) He and (b) 1.6% H_2O/He. Note, a lower content of water was used in the X-ray experiments simply due to equipment limitations.

at 2153 cm^{-1} may be assigned to CO on $Z^-Pd^{2+}Z^-$ as this peak exists in both spectra, and is thus stable in the presence of CO and H_2O, which would be consistent with the reactor data presented above. Finally, peaks at 2138 and 2120 cm^{-1} are observed in spectrum (a). These peaks can be also assigned to CO-Pd^{2+} [41,47]. The configuration of the Pd^{2+} species associated with the peaks at 2138 and 2120 cm^{-1} is likely altered in the presence of H_2O, as they do not appear in spectrum (b), but corresponding peaks at 2134 and 2116 cm^{-1} appear. These peaks could be related to CO bound on hydrated Pd^{2+}. In spectrum (b), the peak at 2144 cm^{-1} potentially represents a polycarbonyl Pd^{2+} species due to higher CO loading [50].

Although there are several IR features associated with the ion-exchanged Pd discussed above, it is the IR features in the metallic region that demonstrate clearer change. In the metallic Pd region, spectrum (a) does not display any peaks besides a small feature at 2098 cm^{-1}. This peak, along with a peak at 2078 cm^{-1} are found in spectrum (b) and are assigned to CO-Pd^0 in a linear conformation [41, 47]. Peaks at 1921 and 1954 cm^{-1} arise in spectrum (b), which are assigned to CO-Pd_2^0 in a bridging conformation. Pace et al. have identified pore-confined Pd^0 species and assigned the IR feature at 1950 cm^{-1} to such a species [47]. Due to the evolution of a feature corresponding to these pore-confined Pd particles, one possibility is that the growth of the low temperature NO_x desorption peak after CO + H_2O treatment may be due to NO stored on small Pd^0 clusters formed in the pores during the CO + H_2O pretreatment. This was also suggested by Gu et al. [38] to explain a similar IR phenomenon, as bridging CO-Pd_2 peaks, formed by CO + H_2O exposure over Pd-ZSM-5, decreased in intensity upon NO exposure. They note however that this is not conclusive since CO may simply be desorbing from the Pd^0 clusters but not necessarily replaced by NO. Another possibility is that the NO exposure displaces the bound CO but also breaks apart the clusters leading to the more traditionally bound NO on solvated Pd ions.

3.8. In-Situ XAS – CO + H_2O exposure

In-situ XAS experiments were performed to probe the local environment of Pd in Pd/BEA during low temperature CO + H_2O exposure. Here, the catalysts were exposed to 1000 ppm CO, 1.6% H_2O, 10% O_2 and balance He at 80 °C. The XANES of the PdBEA12.5 sample at the Pd K-edge before and during exposure to CO + H_2O are shown in Fig. 8a. During CO + H_2O exposure, the catalyst displays an absorption edge very similar to that of the Pd foil standard, indicating that most of the Pd is reduced by the exposure. In contrast, before the CO + H_2O exposure, the Pd is completely oxidized by the oxygen pretreatment.

In the EXAFS, Fig. 8b, we observe the formation of a peak corresponding to Pd-Pd scattering after the CO + H_2O exposure, while the peak corresponding to Pd-O scattering diminishes in size. The coordination number of the Pd-Pd peak is lower in the sample (CN=9.0) than that of the foil (CN=12), which indicates that the formed Pd^0 particles are limited in size [68]. These results are consistent with the CO DRIFTS, suggesting that a reduced Pd phase forms during low temperature CO treatment with H_2O.

3.9. NO DRIFTS

To further probe the NO_x storage sites, DRIFTS spectra were collected after exposure to NO and H_2O. On Pd/zeolites, NO_x adsorption generally presents two peaks corresponding to NO bound on Pd active sites. Kim et al. [59] reported peaks at 1860 cm^{-1} and 1810 cm^{-1} after NO exposure to Pd/CHA. They, and other authors [37,38,50,63,69], have assigned the higher wavenumber peak (~1860 cm^{-1}) to NO-Pd^{2+}. The assignment of the second peak (~1810 cm^{-1}), however, is still debated in the literature, with assignment to NO-Pd^+ by some authors [59,63,69], and to NO on a hydrated Pd^{2+} species by others [37,38,50].

Fig. 9 shows the DRIFTS spectra taken with the PdBEA12.5 sample aged 650 °C after exposure to 700 ppm NO in 1.6% H_2O. Here, we observe the growth of peaks centered at 1867 cm^{-1} and 1821 cm^{-1}. The peak at 1821 cm^{-1} increases for 10 min upon NO exposure, and then decreases afterwards. The behavior of this peak suggests that the NO-

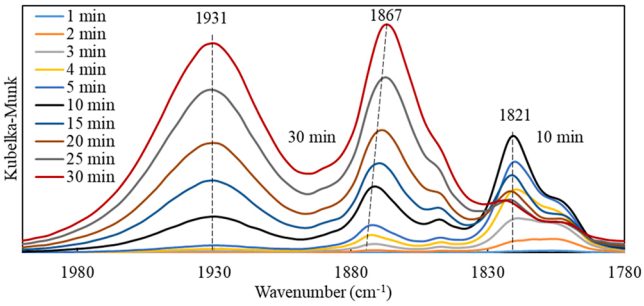

Fig. 9. NO DRIFTS spectra collected over PdBEA12.5 during 30 min exposure at 80 °C to 700 ppm NO in 1.6% H_2O/He.

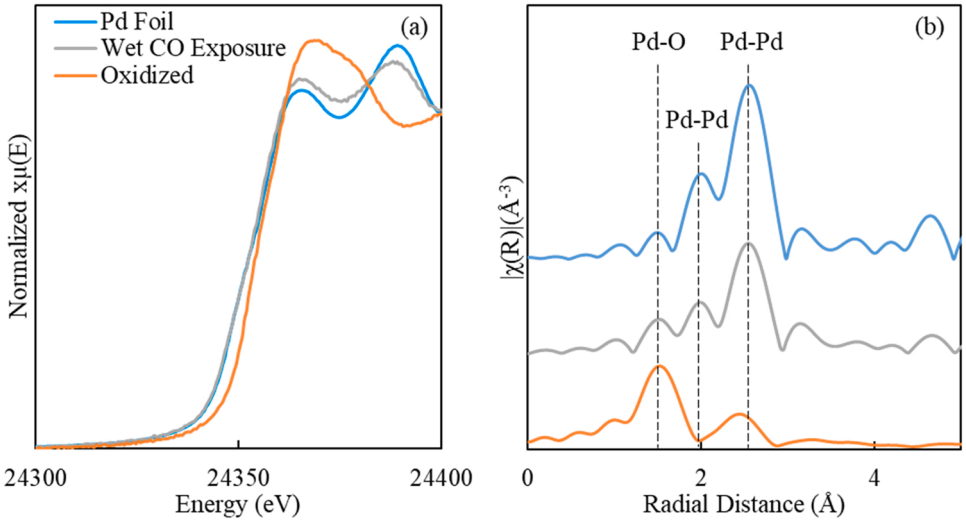

Fig. 8. XAS at the Pd K-edge over PdBEA12.5 before and after exposure to 1000 ppm CO, 1.6% H_2O, 10% O_2, and balance He at 80 °C for 30 min. Note, a lower content of water was used in the X-ray experiments simply due to equipment limitations. The XANES region is shown in (a) and the magnitude of the Fourier-transform of the EXAFS spectra is shown in (b).

Pd^{n+} species responsible for this peak is transiently formed and then converts to another Pd species. This is consistent with the highlighted mechanism, where NO would adsorb to $[Pd(OH)]^+$ and then reduce it to Pd^+ through Eq. (3). Thus, the peak at 1821 cm^{-1} is assigned to NO-$[Pd(OH)]^+$.

With the assignment of an IR feature to NO-$[Pd(OH)]^+$, the presence of $[Pd(OH)]^+$ by itself should be detectable with IR as well. Specifically, the O-H stretching feature in the range of 3650–3670 cm^{-1} should appear when the spectrum of the H-form BEA is subtracted from Pd/BEA [47,70]. For the aged catalysts, we attempted to discern this feature, but an IR feature for extra-framework Al-OH overlaps this range, making detection of Pd-OH by this method inconclusive [67,71,72].

The suggested mechanism also demands the formation of NO-Pd^+ sites, which are not yet accounted for in the IR spectrum. This may be resolved by observing the shift in the peak located at 1873 cm^{-1} from this higher wavenumber at 10 min NO exposure to 1867 cm^{-1} after 30 min NO exposure. Although this shift could be due to a change in the local environment, it might also point to the existence of two peaks: one at ~1873 cm^{-1} assigned to NO-Pd^{2+} and the second at ~1867 cm^{-1} assigned to NO-Pd^+, which would explain the transient behavior of the DRIFTS spectra while remaining consistent with the observed chemistry during adsorption. This assignment of two peaks close in wavenumber for NO-Pd^{2+} and NO-Pd^+ was previously suggested by Mandal et al. [37], where DFT calculations for NO adsorption to Pd/SSZ-13 provided frequencies of 1866 and 1853 cm^{-1} for NO-Pd^{2+} and NO-Pd^+ respectively. Note, these calculations were for Pd exchanged into SSZ-13, whereas we are using BEA, which might lead to differences in the absolute values of the differences. More recently, Kim et al. [59] have also concluded that multiple NO-Pd^{n+} species (n = 1,2) may be contributing to the higher wavenumber (~1860 cm^{-1}) peak in the NO DRIFTS spectrum. An additional peak at 1931 cm^{-1} is found in the spectrum. This may be assigned to N_2O_3 which forms during adsorption from interactions of NO with residual O_2 from the pretreatment. This species was reported to be stable in BEA, but less so in smaller pore zeolites such as SSZ-13 [57].

3.10. In-Situ XAS – NO + H_2O exposure

While exposure to CO in the presence of H_2O caused the formation of a reduced Pd phase in Pd/BEA, our data thus far suggest that exposure to NO in the presence of H_2O should not display the same behavior. To verify, in-situ XAS measurements were performed over the PdBEA12.5 sample before and during exposure to 1000 ppm NO, 1.6% H_2O, 10% O_2, and balance He at 80 °C. Fig. 10a shows the XANES, where the NO + H_2O exposed sample does not resemble that of the Pd foil standard, and rather shows characteristics of the oxidized fresh sample, with the white line intensity falling between that of a freshly oxidized sample and the reduced Pd foil.

Analysis of the EXAFS, Fig. 10b, shows that no peak representing Pd-Pd scattering formed over the NO + H_2O exposed sample indicating that NO adsorption did not result in the formation of Pd^0. The coordination of the Pd-O scattering path diminished when exposed to NO + H_2O with a CN of 1.8 during NO + H_2O exposure versus a CN of 3.8 before the NO + H_2O exposure. Also, there is no longer any second shell scattering in the region of R = 2.4 Å, which corresponds to Pd-O-Si(Al) associated with the zeolite framework. This suggests that the Pd is solvated under the NO + H_2O exposure, and is consistent with previous XAS studies on Pd/zeolites in the presence of water or NO [37,73]. As mentioned above, with exposure to CO + H_2O, a reduced Pd phase forms. This does not preclude that Pd was first solvated before the reduction, however, the steps involved in that transformation are not clear from the results we have.

In-situ XAS measurements during exposure to NO + H_2O were also carried out on the aged catalysts, fittings provided in Table 5. The aged samples displayed a lower Pd–O coordination number when compared to their fresh counterparts. Previously, Okumura et al. reported a similar finding when exposing Pd-ZSM-5 to NO at room temperature. They found that the highly dispersed Pd^{2+} also detached from the ion-exchange site and reduced to form Pd^+ with NO adsorbed [73]. In this

Table 5
EXAFS fittings for PdBEA during exposure to 1000 ppm NO, 1.6% H_2O, 10% O_2, and balance He.

Sample	Treatment	Scattering Pair	CN (+- 10%)	ΔR (+- 0.02 Å)	$\Delta\sigma^2$ ($Å^2$)	E_o Shift (eV)
PdBEA12.5 Fresh	Wet NO 80 °C	Pd-O	1.8	-0.051	0.0013	4.74
PdBEA19 Fresh	Wet NO 80 °C	Pd-O	2.5	-0.049	0.0013	4.70
PdBEA12.5 Aged 650 C	Wet NO 80 °C	Pd-O	1.6	-0.054	0.0013	4.98
PdBEA19 Aged 650 C	Wet NO 80 °C	Pd-O	1.9	-0.054	0.0013	4.95

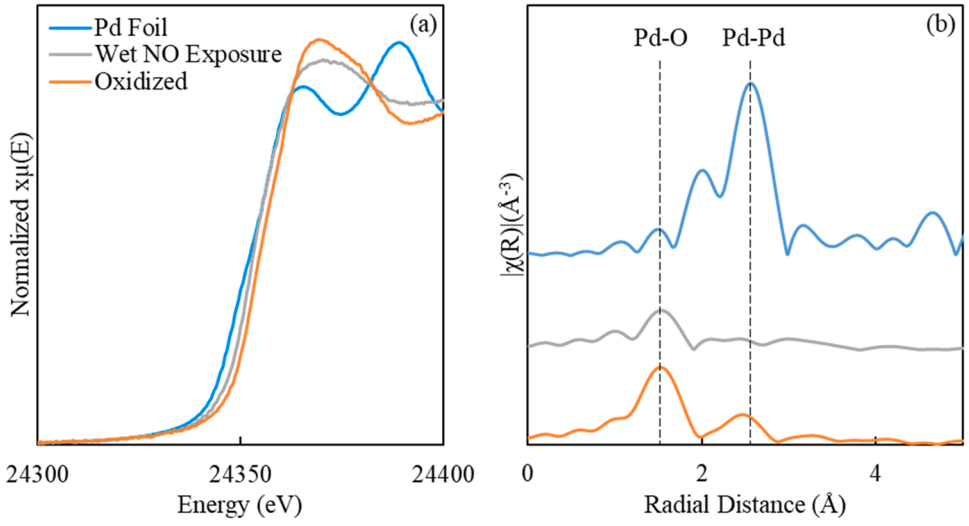

Fig. 10. XAS at the Pd K-edge over PdBEA12.5 before and after exposure to 1000 ppm NO, 1.6% H_2O, 10% O_2, and balance He at 80 °C for 30 min. The XANES region is shown in (a) and the magnitude of the Fourier-transform of the EXAFS spectra is shown in (b).

model, Pd^{+} is only associated with one NO molecule. Therefore, the lower first shell Pd-O intensity for the aged samples can be attributed to their higher fraction of Pd^{+}, consistent with the NO_x TPD results. It follows that the decrease in Pd-O first shell intensity after HTA is associated with the formation of additional partially reduced Pd^{2+} sites, i.e., Pd^{+}.

3.11. Pd speciation in relation to HC trap behavior

In the presence of H_2O, ethylene trapping on Pd/zeolites occurs primarily on ionic Pd active sites as a chemisorption process followed by oligomerization [27]. In Fig. 1, the hydrothermally aged catalysts showed a decline in ethylene adsorption capacity for all three Si/Al ratios. Loss of Pd active sites via Pd agglomeration during aging was ruled out since there was an observed increase in NO_x adsorption after aging conditions. Characterization results instead showed a transformation, by HTA, from mainly non-reducible Pd^{2+} sites to $[Pd(OH)]^{+}$ sites. It follows that the loss in ethylene uptake after HTA was due to the lower activity of $[Pd(OH)]^{+}$ versus Pd^{2+} in the ethylene adsorption or oligomerization process.

Ethylene oxidation activity also decreased with increasing HTA severity. Qualitatively, there was a change in the shape of the conversion versus temperature profile between the fresh catalyst to the aged catalysts, Fig. 2, with the fresh catalyst not displaying a traditional S-shaped curve. All catalysts, however, displayed CH_3CHO selectivity at low conversions, which is typical of Wacker oxidation [35,36]. This behavior is indicative of Pd^{2+} contributing to the oxidation. The current results suggest that $[Pd(OH)]^{+}$ is less active in ethylene oxidation than Pd^{2+}. However, with a change in the amount of particulate Pd also occurring via increased ion-exchange evidence with HTA, it may also play a role in the hydrocarbon oxidation.

4. Conclusions

Pd/BEA hydrocarbon traps with three Si/Al ratios were evaluated before and after HTA. Less ethylene was adsorbed by the catalysts after HTA, while NO_x storage increased. XAS characterization provided no evidence of a major PdO phase after aging which, along with the observed increase in NO adsorption, demonstrates that initially-present Pd^{2+} active sites did not convert to agglomerated PdO domains.

NO_x TPD experiments showed two main desorption peaks, a low temperature peak which exists for the fresh catalyst and assigned to Pd^{2+}, and a high temperature peak which exists for aged catalysts assigned to $[Pd(OH)]^{+}$. The latter peak increases in area with HTA. Removal of the reducible $[Pd(OH)]^{+}$ active sites by a CO and H_2O treatment at 80 °C isolated the low temperature NO_x desorption peak and further verified that the high temperature peak is associated with a reducible Pd species. DRIFTS studies, which replicate the CO and H_2O pretreatment, identified Pd^{2+} as the species responsible for the low temperature NO_x desorption peak. DRIFTS experiments with NO adsorption in the presence of H_2O revealed a transient feature which we assigned to NO-$[Pd(OH)]^{+}$. This feature declined in intensity upon continued exposure, and another arose, which was assigned to NO-Pd^{+}. In-situ XAS experiments further validated the assertion that at 80 °C even in a lean environment, CO + H_2O exposure can completely reduce $[Pd(OH)]^{+}$ to Pd^{0}, while NO + H_2O exposure does not lead to the formation of Pd^{0}. Instead, NO + H_2O exposure led to a decline in the Pd-O first shell intensity and the detachment of the Pd from the ion-exchange site. The aged catalysts contained even lower first shell intensity when exposed to NO + H_2O, suggesting a higher fraction of Pd^{+} under reaction conditions. This implies that the aged samples contain a higher fraction of $[Pd(OH)]^{+}$ initially. Because of this, we propose that Pd^{2+} is more active than $[Pd(OH)]^{+}$ in ethylene oligomerization, the main mechanism of ethylene storage. It also follows that Pd^{2+} is more active in ethylene oxidation than $[Pd(OH)]^{+}$.

CRediT authorship contribution statement

Ryan P. Zelinsky: Conceptualization, Methodology, Formal analysis, Investigation, Writing – original draft, Visualization **David P. Dean:** Formal analysis, Investigation. **Christian J. Breckner:** Formal analysis, Investigation. **Silvia Marino:** Investigation. **Jeffrey T. Miller:** Formal analysis, Investigation, Supervision. **William S. Epling:** Conceptualization, Methodology, Formal analysis, Writing – review & editing, Project administration, Funding acquisition, Supervision.

Declaration of Competing Interest

The authors declare the following financial interests/personal relationships which may be considered as potential competing interests: William Epling reports financial support was provided by US Department of Energy. Corresponding author is on the editorial board of Applied Catalysis B: Environmental.

Data Availability

Data will be made available on request.

Acknowledgements

This research was funded by the Department of Energy, Vehicle Technologies Office, United States, grant number DE-EE0008233.

This research used resources of the Advanced Photon Source, a U.S. Department of Energy (DOE) Office of Science user facility operated for the DOE Office of Science by Argonne National Laboratory under Contract No. DE-AC02–06CH1135. MRCAT operations and the beamline 10-BM were supported by the Department of Energy and the MRCAT member institutions.

The Empyrean X-ray Diffractometer instrument within UVA's Nanoscale Materials Characterization Facility (NMCF) was used.

Appendix A. Supporting information

Supplementary data associated with this article can be found in the online version at doi:10.1016/j.apcatb.2022.121938.

References

[1] A. Wimmer, H. Eichlseder, M. Klell, G. Figer, Potential of HCCI concepts for DI diesel engines, Int. J. Veh. Des. 41 (2006) 32–48, https://doi.org/10.1504/ijvd.2006.009660.
[2] M.P.B. Musculus, P.C. Miles, L.M. Pickett, Conceptual Models for Partially Premixed Low-temperature Diesel Combustion, Elsevier Ltd, 2013, https://doi.org/10.1016/j.pecs.2012.09.001.
[3] D. Han, A.M. Ickes, S.V. Bohac, Z. Huang, D.N. Assanis, HC and CO emissions of premixed low-temperature combustion fueled by blends of diesel and gasoline, Fuel 99 (2012) 13–19, https://doi.org/10.1016/j.fuel.2012.04.010.
[4] R.M. Heck, R.J. Farrauto, Automobile exhaust catalysts, Appl. Catal. Gen. 221 (2001) 443–457, https://doi.org/10.1016/S0926-860X(01)00818-3.
[5] J.K. Hochmuth, P.L. Burk, C. Tolentino, M.J. Mignano, Hydrocarbon traps for controlling cold start emissions, SAE Tech. Pap. (1993) 205–218, https://doi.org/10.4271/930739.
[6] E.R. Becker, R.J. Watson, Future trends in automotive emission control, SAE Tech. Pap. Ser. (1998), 980413.
[7] A. Russell, W.S. Epling, Diesel oxidation catalysts, Catal. Rev. - Sci. Eng. 53 (2011) 337–423, https://doi.org/10.1080/01614940.2011.596429.
[8] Y.-F.Y. Yao, Oxidation of alkanes over noble metal catalysts, Ind. Eng. Chem. Prod. Res. Dev. 19 (1980) 293–298, https://doi.org/10.1021/i360075a003.
[9] F. Diehl, J. Barbier, D. Duprez, I. Guibard, G. Mabilon, Catalytic oxidation of heavy hydrocarbons over Pt/Al2O3. Influence of the structure of the molecule on its reactivity, Appl. Catal. B Environ. 95 (2010) 217–227, https://doi.org/10.1016/j.apcatb.2009.12.026.
[10] M.J. Heimrich, L.R. Smith, J. Kitowski, Cold-start hydrocarbon collection for advanced exhaust emission control, SAE Tech. Pap. (1992) 1–12, https://doi.org/10.4271/920847.
[11] F. Miano, Adsorption of hydrocarbon vapour mixtures onto zeolite 5A, Colloids Surf. Physicochem. Eng. Asp. 110 (1996) 95–104, https://doi.org/10.1016/0927-7757(95)03439-0.
[12] D.W. Breck, Zeolite molecular sieves: structure, chemistry, and use, 1973.

[13] N.R. Burke, D.L. Trimm, R.F. Howe, The effect of silica:alumina ratio and hydrothermal ageing on the adsorption characteristics of BEA zeolites for cold start emission control, Appl. Catal. B Environ. 46 (2003) 97–104, https://doi.org/10.1016/S0926-3373(03)00181-4.
[14] B. Azambre, A. Westermann, G. Finqueneisel, F. Can, J.D. Comparot, Adsorption and desorption of a model hydrocarbon mixture over HY zeolite under dry and wet conditions, J. Phys. Chem. C 119 (2015) 315–331, https://doi.org/10.1021/jp509046n.
[15] J.H. Park, S.J. Park, H.A. Ahn, I.S. Nam, G.K. Yeo, J.K. Kil, Y.K. Youn, Promising zeolite-type hydrocarbon trap catalyst by a knowledge-based combinatorial approach, Microporous Mesoporous Mater. 117 (2009) 178–184, https://doi.org/10.1016/j.micromeso.2008.06.021.
[16] J. Nunan, J. Lupescu, G. Denison, D. Ball, D. Moser, HC traps for gasoline and ethanol applications, SAE Tech. Pap. 2 (2013) 430–449, https://doi.org/10.4271/2013-01-1297.
[17] J.A. Lupescu, T.B. Chanko, J.F. Richert, J.E. Devries, Treatment of vehicle emissions from the combustion of E85 and gasoline with catalyzed hydrocarbon traps, SAE Tech. Pap. (2009) 485–496, https://doi.org/10.4271/2009-01-1080.
[18] X. Liu, J.K. Lampert, D.A. Arendarskiia, R.J. Farrauto, FT-IR spectroscopic studies of hydrocarbon trapping in Ag+-ZSM-5 for gasoline engines under cold-start conditions, Appl. Catal. B Environ. 35 (2001) 125–136, https://doi.org/10.1016/S0926-3373(01)00247-8.
[19] R. Jonsson, P.H. Ho, A. Wang, M. Skoglundh, L. Olsson, The Impact of Lanthanum and Zeolite Structure on Hydrocarbon Storage, Catalysts 11 (2021) 635, https://doi.org/10.3390/catal11050635.
[20] E.A. Kyriakidou, J. Lee, J.S. Choi, M. Lance, T.J. Toops, A comparative study of silver- and palladium-exchanged zeolites in propylene and nitrogen oxide adsorption and desorption for cold-start applications, Catal. Today (2020), https://doi.org/10.1016/j.cattod.2020.05.019.
[21] C. Horvatits, D. Li, M. Dupuis, E.A. Kyriakidou, E.A. Walker, Ethylene and water co-adsorption on Ag/SSZ-13 zeolites: a theoretical study, J. Phys. Chem. C 124 (2020) 7295–7306, https://doi.org/10.1021/acs.jpcc.0c00849.
[22] S.B. Kang, C. Kalamaras, V. Balakotaiah, W. Epling, Hydrocarbon trapping over Ag-Beta zeolite for cold-start emission control, Catal. Lett. 147 (2017) 1355–1362, https://doi.org/10.1007/s10562-017-2044-2.
[23] R. Zelinsky, W. Epling, Effects of multicomponent hydrocarbon feed on hydrocarbon adsorption–desorption and oxidation light-off behavior on a Pd/BEA hydrocarbon trap, Catal. Lett. 149 (2019) 3194–3202, https://doi.org/10.1007/s10562-019-02888-3.
[24] R. Zelinsky, W.S. Epling, Effects of co and h2o co-feed on the adsorption and oxidation properties of a pd/bea hydrocarbon trap, Catalysts 11 (2021) 1–14, https://doi.org/10.3390/catal11030348.
[25] S.A. Malamis, M.P. Harold, W.S. Epling, Coupled NO and C3H6 trapping, release and conversion on Pd/BEA: evaluation of the lean hydrocarbon NOx trap, Ind. Eng. Chem. Res. 58 (2019) 22912–22923, https://doi.org/10.1021/acs.iecr.9b04919.
[26] J. Lupescu, L. Xu, H.W. Jen, A. Harwell, J. Nunan, C. Alltizer, G. Denison, A new catalyzed HC trap technology that enhances the conversion of gasoline fuel cold-start emissions, SAE Int. J. Fuels Lubr. 11 (2018), https://doi.org/10.4271/2018-01-0938.
[27] L. Xu, J. Lupescu, J. Ura, A. Harwell, W.A. Paxton, J. Nunan, C. Alltizer, Benefits of Pd doped zeolites for cold start HC/NOx emission reductions for gasoline and E85 fueled vehicles, SAE Int. J. Fuels Lubr. 11 (2018) 301–317, https://doi.org/10.4271/2018-01-0948.
[28] L. Xu, J. Lupescu, G. Cavataio, K. Guo, H. Jen, The impacts of Pd in BEA zeolite on decreasing cold-start NMOG emission of an E85 fuel vehicle, SAE Int. J. Fuels Lubr. 11 (2018) 239–246, https://doi.org/10.4271/04-11-03-0013.
[29] T.J. Toops, A.J. Binder, P. Kunal, E.A. Kyriakidou, J.-S. Choi, Analysis of ion-exchanged ZSM-5, BEA, and SSZ-13 zeolite trapping materials under realistic exhaust conditions, Catalysts 11 (2021) 449, https://doi.org/10.3390/catal11040449.
[30] S.A. Malamis, M.P. Harold, Optimizing the lean hydrocarbon NOx trap: Sequential and dual-layer configurations, Catal. Today 360 (2021) 388–400, https://doi.org/10.1016/j.cattod.2020.01.025.
[31] E. Jang, L. Choi, J. Kim, Y. Jeong, H. Baik, C.Y. Kang, C.H. Kim, K.-Y. Lee, J. Choi, A copper-impregnated BEA zeolite for adsorption and oxidation of aromatic species during vehicle cold starts, Appl. Catal. B Environ. 287 (2021), 119951, https://doi.org/10.1016/j.apcatb.2021.119951.
[32] K. Barbera-Italiano, E. Jeudy, M. Lecompte, E. Laigle, C. Norsic, C. Chaillou, G. Bourhis, Trap efficiency of exhaust gas pollutants in microporous sorbents under representative driving conditions, Appl. Catal. B Environ. 304 (2022), 120962, https://doi.org/10.1016/j.apcatb.2021.120962.
[33] I. Friberg, A.H. Clark, P.H. Ho, N. Sadokhina, G.J. Smales, J. Woo, X. Auvray, D. Ferri, M. Nachtegaal, O. Kröcher, L. Olsson, Structure and performance of zeolite supported Pd for complete methane oxidation, Catal. Today 382 (2021) 3–12, https://doi.org/10.1016/j.cattod.2020.11.026.
[34] I. Friberg, N. Sadokhina, L. Olsson, The effect of Si/Al ratio of zeolite supported Pd for complete CH4 oxidation in the presence of water vapor and SO_2, Appl. Catal. B Environ. 250 (2019) 117–131, https://doi.org/10.1016/j.apcatb.2019.03.005.
[35] J. Imbao, J.A. van Bokhoven, A. Clark, M. Nachtegaal, Elucidating the mechanism of heterogeneous Wacker oxidation over Pd-Cu/zeolite Y by transient XAS, Nat. Commun. 11 (2020) 1–9, https://doi.org/10.1038/s41467-020-14982-x.
[36] J. Imbao, J.A. Van Bokhoven, M. Nachtegaal, Optimization of a heterogeneous Pd-Cu/zeolite y Wacker catalyst for ethylene oxidation, Chem. Commun. 56 (2020) 1377–1380, https://doi.org/10.1039/c9cc08835k.
[37] K. Mandal, Y. Gu, K.S. Westendorff, S. Li, J.A. Pihl, L.C. Grabow, W.S. Epling, C. Paolucci, Condition-dependent Pd speciation and NO adsorption in Pd/zeolites, ACS Catal. 10 (2020) 12801–12818, https://doi.org/10.1021/acscatal.0c03585.
[38] Y. Gu, S. Sinha Majumdar, J.A. Pihl, W.S. Epling, Investigation of NO adsorption and desorption phenomena on a Pd/ZSM-5 passive NOx adsorber, Appl. Catal. B Environ. 298 (2021), 120561, https://doi.org/10.1016/j.apcatb.2021.120561.
[39] Y. Gu, R.P. Zelinsky, Y.R. Chen, W.S. Epling, Investigation of an irreversible NOx storage degradation Mode on a Pd/BEA passive NOx adsorber, Appl. Catal. B Environ. 258 (2019), 118032, https://doi.org/10.1016/j.apcatb.2019.118032.
[40] D. Mei, F. Gao, J. Szanyi, Y. Wang, Mechanistic insight into the passive NOx adsorption in the highly dispersed Pd/HBEA zeolite, Appl. Catal. Gen. 569 (2019) 181–189, https://doi.org/10.1016/j.apcata.2018.10.037.
[41] Y. Zheng, L. Kovarik, M.H. Engelhard, Y. Wang, Y. Wang, F. Gao, J. Szanyi, Low-temperature Pd/zeolite passive NOx adsorbers: structure, performance, and adsorption chemistry, J. Phys. Chem. C 121 (2017) 15793–15803, https://doi.org/10.1021/acs.jpcc.7b04312.
[42] H.Y. Chen, J.E. Collier, D. Liu, L. Mantarosie, D. Durán-Martín, V. Novák, R. R. Rajaram, D. Thompsett, Low temperature NO storage of zeolite supported Pd for low temperature diesel engine emission control, Catal. Lett. 146 (2016) 1706–1711, https://doi.org/10.1007/s10562-016-1794-6.
[43] K. Khivantsev, X. Wei, L. Kovarik, N. Jaegers, E. Walter, P. Tran, Y. Wang, J. Szanyi, Pd/FER vs Pd/SSZ-13 Passiv. NOx Adsorbers: Adsorbate-Control. Locat. At. Dispersed Pd(II) FER Determines High. Act. Stab. 2020 1 18 doi: 10.26434/chemrxiv.12385577.
[44] J. Lee, J.R. Theis, E.A. Kyriakidou, Vehicle emissions trapping materials: Successes, challenges, and the path forward, Appl. Catal. B Environ. 243 (2019) 397–414, https://doi.org/10.1016/j.apcatb.2018.10.069.
[45] K. Khivantsev, F. Gao, L. Kovarik, Y. Wang, J. Szanyi, Molecular level understanding of how oxygen and carbon monoxide improve NOx storage in palladium/SSZ-13 passive NOx adsorbers: the role of NO+ and Pd(II)(CO)(NO) Species, J. Phys. Chem. C 122 (2018) 10820–10827, https://doi.org/10.1021/acs.jpcc.8b01007.
[46] A. Vu, J. Luo, J. Li, W.S. Epling, Effects of CO on Pd/BEA passive NOx adsorbers, Catal. Lett. 147 (2017) 745–750, https://doi.org/10.1007/s10562-017-1976-x.
[47] R.B. Pace, T.M. Lardinois, Y. Ji, R. Gounder, O. Heintz, M. Crocker, Effects of treatment conditions on Pd speciation in CHA and beta zeolites for passive NOxadsorption, ACS Omega 6 (2021) 29471–29482, https://doi.org/10.1021/acsomega.1c03440.
[48] Y.S. Ryou, J. Lee, Y. Kim, S. Hwang, H. Lee, C.H. Kim, D.H. Kim, Effect of reduction treatments (H2 vs. CO) on the NO adsorption ability and the physicochemical properties of Pd/SSZ-13 passive NOx adsorber for cold start application, Appl. Catal. Gen. 569 (2019) 28–34, https://doi.org/10.1016/j.apcata.2018.10.016.
[49] J.R. Theis, J.A. Ura, Assessment of zeolite-based Low temperature NOx adsorbers: effect of reductants during multiple sequential cold starts, Catal. Today (2020), https://doi.org/10.1016/j.cattod.2020.01.040.
[50] I. Song, K. Khivantsev, Y. Wang, J. Szanyi, Elucidating the role of CO in the NO storage mechanism on Pd/SSZ-13 with in situ DRIFTS, J. Phys. Chem. C (2022), https://doi.org/10.1021/acs.jpcc.1c10163.
[51] Y.S. Ryou, J. Lee, S.J. Cho, H. Lee, C.H. Kim, D.H. Kim, Activation of Pd/SSZ-13 catalyst by hydrothermal aging treatment in passive NO adsorption performance at low temperature for cold start application, Appl. Catal. B Environ. 212 (2017) 140–149, https://doi.org/10.1016/j.apcatb.2017.04.077.
[52] J. Lee, Y. Ryou, S. Hwang, Y. Kim, S.J. Cho, H. Lee, C.H. Kim, D.H. Kim, Comparative study of the mobility of Pd species in SSZ-13 and ZSM-5, and its implication for their activity as passive NO: X adsorbers (PNAs) after hydro-thermal aging, Catal. Sci. Technol. 9 (2019) 163–173, https://doi.org/10.1039/c8cy02088d.
[53] K. Khivantsev, N.R. Jaegers, L. Kovarik, J.Z. Hu, F. Gao, Y. Wang, J. Szanyi, Palladium/Zeolite low temperature passive NOx adsorbers (PNA): structure-adsorption property relationships for hydrothermally aged PNA materials, Emiss. Control Sci. Technol. 6 (2020) 126–138, https://doi.org/10.1007/s40825-019-00139-w.
[54] J. Kou, J.Z. Chen, J. Gao, X. Zhang, J. Zhu, A. Ghosh, W. Liu, A.J. Kropf, D. Zemlyanov, R. Ma, X. Guo, A.K. Datye, G. Zhang, L. Guo, J.T. Miller, Structural and catalytic properties of isolated Pt2+ sites in platinum phosphide (PTP2), ACS Catal. 11 (2021) 13496–13509, https://doi.org/10.1021/acscatal.1c03970.
[55] A.K. Ghosh, L. Kevan, Catalytic and ESR studies of ethylene dimerization on palladium-exchanged Na-X and Ca-X zeolites, J. Phys. Chem. 92 (1988) 4439–4446, https://doi.org/10.1021/j100326a039.
[56] R. Villamaina, U. Iacobone, I. Nova, E. Tronconi, M.P. Ruggeri, L. Mantarosie, J. Collier, D. Thompsett, Mechanistic insight in NO trapping on Pd/Chabazite systems for the low-temperature NOx removal from Diesel exhausts, Appl. Catal. B Environ. 284 (2021), 119724, https://doi.org/10.1016/j.apcatb.2020.119724.
[57] K. Khivantsev, N.R. Jaegers, L. Kovarik, S. Prodinger, M.A. Derewinski, Y. Wang, F. Gao, J. Szanyi, Palladium/Beta zeolite passive NOx adsorbers (PNA): clarification of PNA chemistry and the effects of CO and zeolite crystallite size on PNA performance, Appl. Catal. Gen. 569 (2019) 141–148, https://doi.org/10.1016/j.apcata.2018.10.021.
[58] M. Ambast, K. Karinshak, B.M.M. Rahman, L.C. Grabow, M.P. Harold, Passive NOx adsorption on Pd/H-ZSM-5: Experiments and modeling, Appl. Catal. B Environ. 269 (2020), 118802, https://doi.org/10.1016/j.apcatb.2020.118802.
[59] P. Kim, J. Van der Mynsbrugge, H. Aljama, T.M. Lardinois, R. Gounder, M. Head-Gordon, A.T. Bell, Investigation of the modes of NO adsorption in Pd/H-CHA, Appl. Catal. B Environ. 304 (2022), 120992, https://doi.org/10.1016/j.apcatb.2021.120992.

[60] K.I. Shimizu, Y. Kamiya, K. Osaki, H. Yoshida, A. Satsuma, The average Pd oxidation state in Pd/SiO 2 quantified by L 3-edge XANES analysis and its effects on catalytic activity for CO oxidation, Catal. Sci. Technol. 2 (2012) 767–772, https://doi.org/10.1039/c2cy00422d.
[61] B.J. Adelman, W.M.H. Sachtler, The effect of zeolitic protons on NO(x) reduction over Pd/ZSM-5 catalysts, Appl. Catal. B Environ. 14 (1997) 1–11, https://doi.org/10.1016/S0926-3373(97)00007-6.
[62] B. Zhang, M. Shen, J. Wang, J. Wang, J. Wang, Investigation of various pd species in Pd/BEA for cold start application, Catalysts 9 (2019), https://doi.org/10.3390/catal9030247.
[63] A. Gupta, S. Bong, M.P. Harold, NOx uptake and release on Pd / SSZ-13: Impact Of Feed composition and temperature, Catal. Today (2020) 0–1, https://doi.org/10.1016/j.cattod.2020.01.018.
[64] C. Descorme, P. Gélin, M. Primet, C. Lécuyer, Infrared study of nitrogen monoxide adsorption on palladium ion-exchanged ZSM-5 catalysts, Catal. Lett. 41 (1996) 133–138, https://doi.org/10.1007/BF00811479.
[65] S. Shwan, R. Nedyalkova, J. Jansson, J. Korsgren, L. Olsson, M. Skoglundh, Hydrothermal stability of Fe-BEA as an NH 3-SCR catalyst, Ind. Eng. Chem. Res. 51 (2012) 12762–12772, https://doi.org/10.1021/ie301516z.
[66] K. Khivantsev, N.R. Jaegers, I.Z. Koleva, H.A. Aleksandrov, L. Kovarik, M. Engelhard, F. Gao, Y. Wang, G.N. Vayssilov, J. Szanyi, Stabilization of super electrophilic Pd+2 cations in small-pore SSZ-13 zeolite, J. Phys. Chem. C (2019), https://doi.org/10.1021/acs.jpcc.9b06760.
[67] A.W. Aylor, L.J. Lobree, J.A. Reimer, A.T. Bell, Investigations of the dispersion of Pd in H-ZSM-5, J. Catal. 172 (1997) 453–462, https://doi.org/10.1006/jcat.1997.1893.
[68] J.T. Miller, A.J. Kropf, Y. Zha, J.R. Regalbuto, L. Delannoy, C. Louis, E. Bus, J. A. van Bokhoven, The effect of gold particle size on Au{single bond}Au bond length and reactivity toward oxygen in supported catalysts, J. Catal. 240 (2006) 222–234, https://doi.org/10.1016/j.jcat.2006.04.004.
[69] H. Zhao, X. Chen, A. Bhat, Y. Li, J.W. Schwank, Insight into hydrothermal aging effect on deactivation of Pd/SSZ-13 as low-temperature NO adsorption catalyst: effect of dealumination and Pd mobility, Appl. Catal. B Environ. 286 (2021), 119874, https://doi.org/10.1016/j.apcatb.2020.119874.
[70] C. Paolucci, A.A. Parekh, I. Khurana, J.R. Di Iorio, H. Li, J.D. Albarracin Caballero, A.J. Shih, T. Anggara, W.N. Delgass, J.T. Miller, F.H. Ribeiro, R. Gounder, W. F. Schneider, Catalysis in a cage: condition-dependent speciation and dynamics of exchanged Cu cations in SSZ-13 zeolites, J. Am. Chem. Soc. 138 (2016) 6028–6048, https://doi.org/10.1021/jacs.6b02651.
[71] P.H. Ho, J. Woo, R.F. Ilmasani, M.A. Salam, D. Creaser, L. Olsson, The effect of Si/Al ratio on the oxidation and sulfur resistance of beta zeolite-supported Pt and Pd as diesel oxidation catalysts, ACS Eng. Au (2021), https://doi.org/10.1021/acsengineeringau.1c00016.
[72] A. Vimont, F. Thibault-Starzyk, J.C. Lavalley, Infrared spectroscopic study of the acidobasic properties of beta zeolite, J. Phys. Chem. B 104 (2000) 286–291, https://doi.org/10.1021/jp992550t.
[73] K. Okumura, J. Amano, N. Yasunobu, M. Niwa, X-ray absorption fine structure study of the formation of the highly dispersed PdO over ZSM-5 and the structural change of pd induced by adsorption of NO, J. Phys. Chem. B 104 (2000) 1050–1057, https://doi.org/10.1021/jp993182w.